How to enable large format 4680 cylindrical lithium-ion batteries

Shen Li [a,c,1], Mohamed Waseem Marzook [a], Cheng Zhang [b], Gregory J. Offer [a,c], Monica Marinescu [a,c,*]

[a] *Department of Mechanical Engineering, Imperial College London, London SW7 2AZ, United Kingdom*
[b] *Institute for Future Transport and Cities, Coventry University, Coventry CV1 5FB, United Kingdom*
[c] *The Faraday Institution, Harwell Science and Innovation Campus, Didcot OX11 0RA, United Kingdom*

HIGHLIGHTS

- Distributed 3D electro-thermal model built for cylindrical cells with true structure.
- The ability to thermally manage cylindrical cells limits their maximum size.
- Surface to volume ratio and inner structure are critical to cell performance.
- Large cylindrical cells must be base cooled and have continuous tabs.
- For small cylindrical cells side cooling is most efficient.

ARTICLE INFO

ABSTRACT

The demand for large format lithium-ion batteries is increasing, because they can be integrated and controlled easier at a system level. However, increasing the size leads to increased heat generation risking overheating. 1865 and 2170 cylindrical cells can be both base cooled or side cooled with reasonable efficiency. Large format 4680 cylindrical cells have become popular after Tesla filed a patent. If these cells are to become widely used, then understanding how to thermally manage them is essential. In this work, we create a model of a 4680 cylindrical cell, and use it to study different thermal management options. Our work elucidates the comprehensive mechanisms how the hot topic 'tabless design' improves the performance of 4680 cell and makes any larger format cell possible while current commercial cylindrical cells cannot be simply scaled up to satisfy power and thermal performance. As a consequence, the model identifies the reason for the tabless cell's release: the thermal performance of the 4680 tabless cell can be no worse than that of the 2170 cell, while the 4680 tabless tab cell boasts 5.4 times the energy and 6.9 times the power. Finally, via the model, a procedure is proposed for choosing the thermal management for large format cylindrical cell for maximum performance. As an example, we demonstrate that the best cooling approach for the 4680 tabless cell is base cooling, while for the 2170 LG M50T cell it is side cooling. We conclude that any viable large format cylindrical cell must include a continuous tab (or 'tabless') design and be cooled through its base when in a pack. The results are of immediate interest to both cell manufacturers and battery pack designers, while the developed modelling and parameterization framework is of wider use for all energy storage system design.

1. Introduction and motivation

Lithium-ion batteries (LIBs) are a popular energy storage solution due to their high energy and power density, low self-discharge rate and long cycle life [1]. To further reduce both the economic and environmental costs associated with LIBs, there is a strong need to improve the performance efficiency of LIBs throughout their lifetime.

In recent years, large format lithium-ion batteries have been developed for applications such as electric vehicles [2–6]. Large format cells have a number of advantages over smaller form factors. Firstly, the number of interconnectors and control circuits in a battery pack can be reduced, avoiding unnecessary energy loss via voltage drop and dissipative heat generation, as well as enhancing the system reliability [7].

Nomenclature

Abbreviations	**Description**
CCC	Cell cooling coefficient
ECN	Equivalent circuit network
ESS	Energy storage system
EV	Electric vehicle
LIB	Lithium-ion battery
MSMD	Multi-scale multi-dimensional
NTGK	Semi-empirical model named by Newman, Tiedemann, Gu and Kwon
P2D	Pseudo two-dimensional
SoC	State of charge
Symbols	**Description (Unit)**
A_{base}	Cell base area (m^2)
CCC_{base}	Cell cooling coefficient under base cooling condition (W·K^{-1})
$\widetilde{CCC}_{base}^{GN}$	Base cooling CCC normalized for geometry (W·K^{-1}·m^{-3})
$\widetilde{CCC}_{base}^{HG}$	Base cooling CCC normalized for heat generation (W·K^{-1}·Ah^{-2}·Ω^{-1})
CCC_{side}	Cell cooling coefficient under side cooling condition (W·K^{-1})
$\widetilde{CCC}_{side}^{GN}$	Side cooling CCC normalized for geometry (W·K^{-1}·m^{-3})
$\widetilde{CCC}_{side}^{HG}$	Side cooling CCC normalized for heat generation (W·K^{-1}·Ah^{-2}·Ω^{-1})
CR	C rate (h^{-1})
h_{insu}	Effective heat transfer coefficient for heat loss through insulation layer (W·m^{-2}·K^{-1})
L	Cell height (m)
λ_{link}	Effective thermal conductivity between the jellyroll base and the metal can (W·m^{-1}·K^{-1})
q	Cell heat generation rate (W)
Q	Cell rated capacity (Ah)
Q_{base}	Heat rejection rate through cell base (W)
Q_{ext}	Heat extraction rate (W)
Q_{gen}	Heat generation rate (W)
Q_{side}	Heat rejection rate through cell side (W)
R	Cell electrical resistance (Ω)
R_0	Instantaneous ohmic resistance (Ω)
S_1	Average temperature integral over time (K·s)
S_2	Temperature difference integral over time (K·s)
t	Time (s)
T_{avg}	Cell volume-averaged temperature (K)
T_{min}	Minimum temperature within cell (K)
T_{max}	Maximum temperature within cell (K)
T_{target}	Target temperature (K)
ΔT	Temperature difference between max and min temperature within cell (K)
ΔT_{avg}	Metric to gauge cell overall cooling rate (K)
ΔT_{axial}	Temperature difference between the top and bottom of the cell can (K)
ΔT_{grad}	Metric to gauge cell emerging thermal gradient (K)
ΔT_{radial}	Temperature difference between the core and the side surface at the cell height mid-point (K)

Secondly, the pack level energy and power density can be higher due to the reduced proportion of casing material [8]. However, a potential disadvantage of large format cells is overheating, when the importance of effective thermal management is overlooked. Without effective heat dissipation, higher internal temperatures and larger thermal gradients can develop inside larger cells [9,10], which can limit performance and accelerate degradation significantly [11].

The heat dissipation rate of a cell is strongly affected by its surface-to-volume ratio and thermal conductivity [12]. For cylindrical cells, the surface-to-volume ratio is inherently poor due to geometry, as it is inversely proportional to the radius. The thermal conductivity is strongly anisotropic, with a low thermal conductivity in the radial direction [13]. Therefore, it is challenging to increase the size of cylindrical cells beyond the until now common diameters of 18 mm (1865 cell) and 21 mm (2170 cell), without compromising their ability to reject heat radially.

Although end cooling of cylindrical cells accesses a smaller surface area, thus leading to a lower surface-to-volume ratio compared to side cooling, it benefits from the relatively high thermal conductivity of the jellyroll in the axial direction [13]. End cooling also has the advantage of a constant surface-to-volume ratio when cylindrical cell designs with increasing radius (but constant height) are considered.

The effectiveness of any standard cooling approach is affected by the quality of the thermal connection between the jellyroll and the can. In cylindrical cells the number of tabs between current collectors in the jellyroll and can have usually been optimized for electrical rather than thermal connection. Numerical studies have shown that the number and position of tabs can affect the heat generated by a cell as a by-product of poor electrical design [14,15].

One solution to mitigate the thermal issues in cylindrical cells is through improved tab design [16]. Single-tab (one tab for the positive current collector and one for the negative current collector) and multi-tab designs are common for existing commercial cylindrical cells. The limitation with such tab designs is caused by the positive feedback

between temperature and current density, leading to the local temperature around the tab being higher than elsewhere, thus increasing the volume averaged temperature and the internal thermal gradients [13]. Prior modelling [14] and experimental work [15] have shown that using more tabs for cylindrical cells acts to reduce heat generation and thermal gradients inside the cell. The continuous tab design has been predicted to efficiently reduce heat generation [14], however, due to manufacturing challenges, no commercial cell with continuous tab had been realized until recently. A patent [17] by Tesla Inc. introduces a solution for the manufacturing of large format tabless 4680 cylindrical cells with a novel 'tabless' design, essentially a continuous tab. Based on model predictions [14], this continuous tab design is expected to overcome the thermal issues associated with large cylindrical cell size through reduced heat generation and increased heat dissipation. The benefit of tabless design on current distribution and temperature for 4680 cells has been demonstrated using a 2D electrochemical jellyroll model [18]. However, factors such as the effect of the current paths through the current collector, the connection between the metal can and the jellyroll and the chosen cooling strategy were not included. These considerations have been shown to be critical in assessing the viability and performance of cylindrical cells [13], but have not been assessed for the 4680 tabless cell.

Thermal management is also known to play a key role in the thermal performance of cylindrical cells [19]. Until recently, the majority of three-dimensional cylindrical cell models [20,21] only included the jellyroll, thus ignoring the internal and external structure of the cell, such as metal can, and the effect of internal thermal connections, such as between the jellyroll and the can. These aspects of the cell design should not be ignored whenever modelling the effect of thermal management [13]. It has been shown that conductive side cooling is the most efficient method for a common 2170 cylindrical cell (model: LG M50T), when considering its jellyroll radius and detailed internal structure [13]. For the newer 4680 continuous tab cell [17], the jellyroll is thicker in the radial direction and the internal structure is different from previous

cylindrical cells. Hence, the most effective cooling strategy for the 4680 cell remains so far unknown.

In order to quantify the effectiveness of cooling on the cell, we calculated the cell cooling coefficient (*CCC*), a previously proposed cell metric designed to quantify the ability to reject heat through different surfaces of a cell [12]. The experimentally measured *CCC* values of commercial pouch cells were found to lie between $0.004 - 0.06 \, WK^{-1}Ah^{-1}$ for tab cooling [12] and between $0.6 - 0.7 \, WK^{-1}Ah^{-1}$ for surface cooling [22], where a larger value of the *CCC* corresponds to improved heat rejection ability. While surface cooling can extract heat more efficiently than tab cooling, it can also lead to accelerated degradation [11,23]. The experimentally measured and modelled surface cooling *CCC* for a prismatic cell was $0.02 - 0.06 \, WK^{-1}Ah^{-1}$ [8], a low value interpreted as due to the cell's large form factor, and thus low surface-to-volume ratio. A recent experimental study reported the base cooling *CCC* is $0.03 \, WK^{-1}Ah^{-1}$ [24] for a commercial 2170 cylindrical cell with single-tab design. There currently is no published value for an experimentally obtained *CCC* on either continuous tab cylindrical cells, or any design of 4680 cells, presumably because they are still not easily available.

To quantitatively investigate the effects of both cell design and thermal management, a cell-level distributed model with detailed internal structure is needed. There are broadly two categories of cell-level models in literature: continuum models and equivalent circuit models. Derived from the pseudo two-dimensional (P2D) physics-based model [25–28], various Multi-Scale Multi-Dimensional (MSMD) models have been proposed to accelerate the simulation from electrochemical sub-domains up to the cell level [14,21,29–32]. Newman, Tiedemann, Gu and Kwon (NTGK) et al. [33–36] pioneered a semi-empirical model to explore many aspects of cell behavior at the cell scale [37–40]. However, these types of models are notoriously difficult to parameterize with confidence [41]. Besides, all aforementioned models do not include the detailed cell internal structure, rather focusing on the amount of active material and interfaces. A recent distributed equivalent circuit network (ECN) model with detailed internal structures [13] has been

demonstrated to predict cylindrical cell electro-thermal performances with relative computational ease and sufficiently high precision.

This study is motivated by the advent of cylindrical cells with increasing format factor, and the ensuing need to design and thermally manage them in an efficient manner. It provides two significant contributions: firstly, it reveals the complete mechanisms through which the 'tabless design' acts as an enhancer and enabler of large format cylindrical cells, and secondly, it describes a procedure to identify the optimal thermal management for any future large format cell that may be built. The manuscript is organized as follows: Section 2 presents the model setup of the distributed electro-thermal ECN model, including detailed internal structures. The role of tab as electrical connectors is explored in Section 3. In Section 4, the model is validated against base cooling cell cooling coefficient (*CCC*) situation. These bespoke experiments were chosen for their suitability to validate the accuracy of the representation in the model of the thermal connections between the jellyroll and metal. Then the benefit from thermal connections is presented in Section 4. In Section 5, the large format cell model is then used as a beginning of life cell design tool, to investigate how to thermally manage the large format cylindrical cells in an effective manner with immediate implication to battery engineering industry. Section 6 concludes this paper.

2. Model description

A cylindrical cell is composed of a jellyroll (current collector, electrodes, separator soaked), internal tabs and the outside metal can filled with electrolyte. Fig. 1 shows the schematic description of cylindrical cells with single and continuous tab (or tabless). The cross-section schematic of a single-tab cylindrical cell is shown in Fig. 1(a). For the single-tab design, the negative side of the jellyroll is electrically and thermally connected to the metal can by the single tab, as illustrated in Fig. 1(b). Fig. 1(d) shows the negative side for the disassembled LG M50T cell. As it can be seen, other than this single tab, the remaining space between the jellyroll base and metal can is filled with separator to
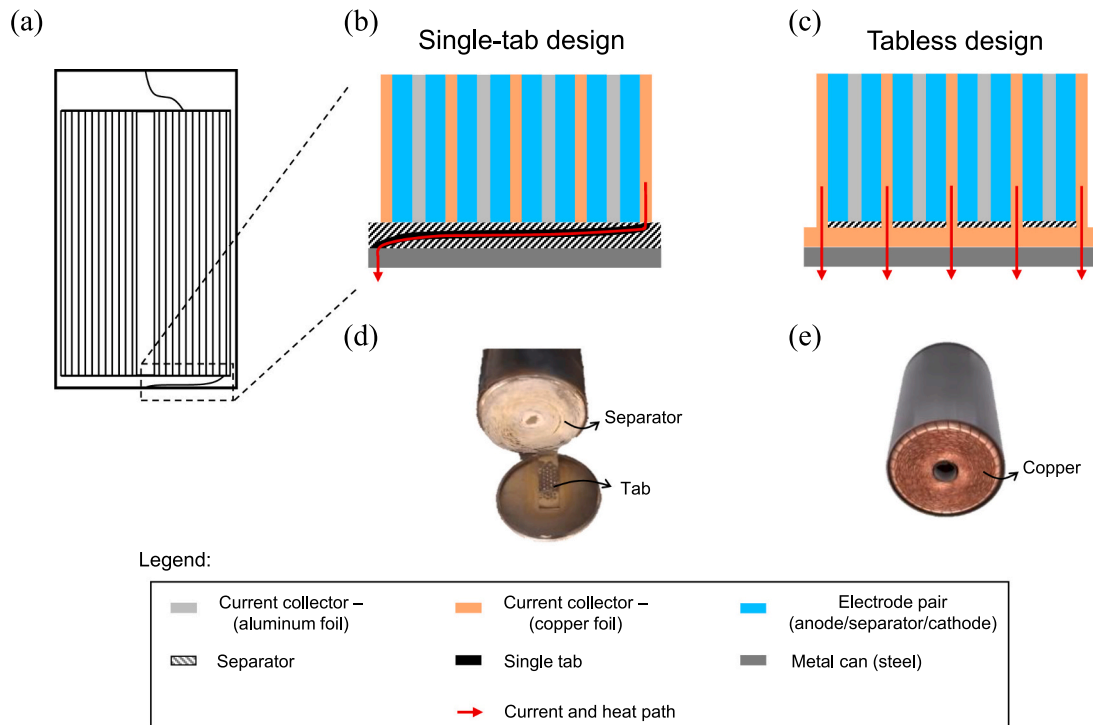

Fig. 1. Cell diagram for the two cylindrical cell designs. (a) Cross section of cylindrical cell with single-tab design. The geometry details between jellyroll and metal can are zoomed in for (b) single-tab design and (c) tabless (or continuous-tab) design. The negative side for (d) an opened 2170 LG M50T cell, obtained experimentally, and (e) a 4680 Tesla tabless cell jellyroll [42].

prevent short-circuit. Since the thermal conductivity of the separator is orders of magnitude lower than that of the metal can and the current collector, this single tab forms the main heat rejection path from the jellyroll base to the outside metal can.

The continuous tab (or tabless) design is sketched in **Fig. 1**(c). In comparison to the single-tab design, the addition of a large number of connection points with the can is expected to greatly reduce the bottleneck for both electrical connection and heat rejection via the base (and cap). **Fig. 1**(e) schematically shows the negative side for the Tesla 4680 cell, from which it can be assumed that the jellyroll base, formed by copper tabs instead of separator, is in direct contact with the can.

Cylindrical cells of two sizes, 2170 and 4680, are modelled using the 3D distributed electro-thermal modelling framework validated in our previous work [13]. The dimensions of the 2170 and 4680 cylindrical cells used in the distributed ECN model are shown in Table 1. The dimensions of the 2170 cell are those of the LG M50T cell. A small mismatch between the reported values of the "real cell" and those in the "model" is caused by imposing the constraint of integer layer number. The ensuing difference in electrode size is similar to errors expected due to electrode and current collector thickness measurements. For a commercially relevant 4680 cell, most required dimensions are not available. A virtual tabless 4680 cell model is built here by assuming that the electrodes' materials and thicknesses are the same as in a LG M50T cell. The rated capacity of the 4680 virtual cell is calculated by scaling the electrode plate area of the 2170 counterpart. As a result, the capacity for the 4680 cell is 5.4 times higher than that of the 2170 cell.

The following tab designs for electrical and thermal contact are studied for the 2170 and 4680 cells, in order to identify their effects on the electrical and thermal bottlenecks to cell performance:

1. Single-tab design. A single negative tab is located at the outermost edge of the negative current collector, and a single positive tab is located a third of the distance from the core to the outer end of the positive current collector. Between the jellyroll and the metal can at the cell base and top, there are two main sources of thermal paths - a separator-metal thermal contact and the tabs. For the 2170 cell, this configuration reflects the structure found inside the LG M50T cell during tear-down. **Fig. 1**(d) shows the tab configuration and separator-metal contact for the negative side.
2. Dual-tab design. The negative current collector has two tabs attached, one placed at each of its end edges. The positive current collector has two tabs attached, one located at a third of the distance from the inner to the outside edge of the positive current collector, and the other tab located at the outermost edge of the current collector. Separator-metal thermal contact between jellyroll and metal can for negative and positive side. **Fig. 3**(a) shows the tab configuration and separator-metal contact for the negative side.
3. All-tab design. This design mimics an electrical connection of tabs without the respective thermal connection. The positive and negative current collectors are electrically connected to the terminals via one tab for each spiral loop. The thermal contact between the

jellyroll and the metal can for the negative and the positive sides is formed by the tab and separator-metal contact. **Fig. 3**(a) shows the tab configuration and separator-metal contact for the negative side.
4. Tabless (continuous-tab) design. The positive and negative current collectors at top/base sides are folded to make plane connections with the plane terminals (metal can top/base sides), as shown in **Fig. 1**(e). The metal-metal thermal contact between the jellyroll and the can is made.

3. The role of tabs as electrical connectors

3.1. Cell voltage performance

The electrical performance of the all-tab and the single-tab designs is studied for both the 2170 and 4680 cells, for a fixed discharge current of 1.5C. This value was chosen as extreme enough to show the effect of tab design, while still within the limits of the LG M50T datasheet. The thermal boundary is in all cases convective cooling on all surfaces with a heat transfer coefficient of 30 $Wm^{-2}K^{-1}$ and ambient temperature of 25 °C.

The discharge performance and thermal behavior of single-tab and all-tab designs of a 2170 cylindrical cell are compared in Fig. 2 for the 1.5C discharge with cut-off voltage of 2.7 V. As shown in **Fig. 2**(a), the discharge voltage of the all-tab design is higher than that of the single-tab design, with an averaged voltage difference of 65.32 mV. This voltage difference is explained by the fact that in the single-tab design there is a longer current pathway through the current collector to the tab and hence the cell has a higher internal resistance. For the same reason, the volume-averaged temperature T_{avg} for the all-tab design (45.85 °C) is lower than that calculated for the single-tab design (49.23°C), as shown in **Fig. 2**(b). The volume-averaged temperature is defined as the weighted average temperatures of all the units in the cell, with the unit thermal mass (or heat capacity) as the weighing factor, thus including the thermally inhomogeneous and anisotropic structure of the cell. The thermal gradient ΔT (i.e. the difference of maximum temperature T_{max} and minimum temperature T_{min} within the jellyroll domain) for both tab designs is compared in **Fig. 2**(c). The cell with all-tab design exhibits lower thermal gradients across the jellyroll than the single-tab one. It has been shown that higher thermal gradients contribute to accelerated degradation [11].

In the thermal model, both irreversible and reversible (entropic) heat generation by the electrodes is considered. Irreversible heat generation is considered for current collectors. The total heat generation from a cell is calculated as the sum over all the sub-elements of a cell. The detailed equations and assumptions are listed in the previous modelling work by Li et al. [13]. The total heat generation from current collectors and the electrode/separator/electrode unit is illustrated in **Fig. 2**(d) during the 1.5C discharge process. The heat generation from the current collectors for the all-tab design is negligible compared with their contribution to heat generation in the single-tab design. For all the usual criteria, such as larger discharge energy, lower average temperature and lower temperature gradient, the all-tab design performs better than the single-tab design.

A similar set of simulation is performed for 4680 cylindrical cells with single-tab, dual-tab and all-tab designs. The schematics for those tab designs are illustrated in **Fig. 3**(a). At first the discharge capacity of single-tab design under different C rates is checked in **Fig. 3**(b). The discharge capacity under 0.1C discharge (pseudo OCV test), is close to the rated capacity (27.07 Ah). The discharge capacity is significantly reduced as the C rate increases from 0.1C to 1.5C. The terminal voltage of this 4680 cell for 1.5C falls below the cutoff voltage of 2.7 V from the start of discharge (**Fig. 3**(b)) unlike the 2170 single-tab cell (**Fig. 2**(a)). This effect can be explained by considering the length of the jellyroll in each of the cells. **Fig. 3**(c) shows the schematic representation of the unwound current collector for the 2170 (single-tab) cell and the 4680 (all three cases of tab designs) cells. When a single-tab design is applied,

Table 1
Features of the model for 2170 and 4680 cell.

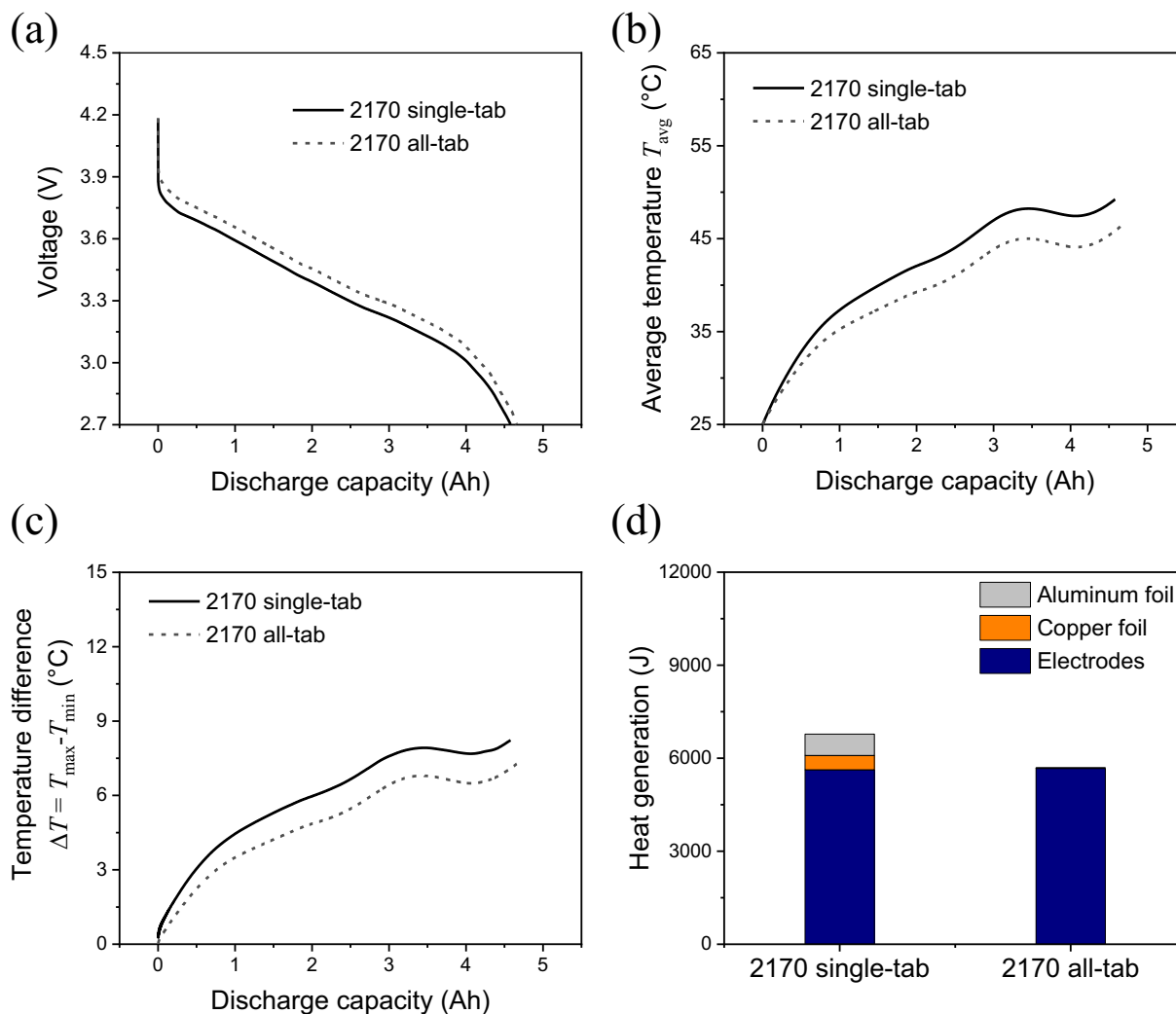| Features	2170 LG M50T (real cell)	2170 LG M50T (model)	4680 'tabless' cell (model)
Cell diameter (mm)	21.00	21.78	46.44
Cell height (mm)	70.00	70.00	80.00
Surface-to-volume ratio (mm^{-1})	0.22	0.22	0.11
Electrode length (mm)	915	884	4183
Electrode plate area (mm^2)	1.22e5	1.17e5	6.33e5
Tab Length/Width/Thickness (mm)	11/3.5/ 0.165	11/3.5/ 0.165	N/A
Rated capacity (Ah)	5.00	5.00	27.07

Fig. 2. Comparison of single-tab and all-tab designs for a 2170 cylindrical cell during 1.5C discharge under convective thermal boundary condition: (a) terminal voltage, (b) volume-averaged jellyroll temperature, (c) maximum temperature difference across the jellyroll and (d) total heat generation of electrodes and current collectors during discharge.

the electrical path (indicated by red arrows in Fig. 3(c)) is significantly longer for the 4680 cell than for the 2170 cell, as the current collector lengths are 4.18 m vs 0.88 m, as given for the electrode lengths in Table 1. Features of the model for 2170 and 4680 cell. The voltage drop at the start of the discharge is hence significant for the single-table 4680, due to its significantly higher resistance.

The all-tab design does not exhibit the capacity limitation for 1.5C discharge, reaching close to full rated capacity as shown in Fig. 3(d). As an intermediate solution, a dual-tab design is also considered. While the discharge capacity of the dual-tab design only approaches 80% of the rated capacity, it performs markedly better than the single-tab design, showing that even adding an extra tab of each polarity can greatly improve performance by reducing internal resistance. These results predict that the electrical performance of the 4680 cell is extremely sensitive to the number of tabs. As illustrated in Fig. 3(c), the long electrical path for the 4680 cell is effectively reduced by increasing the number of tabs (i.e. dual-tab design), with the all-tab design minimizing the electrical path. Unlike for the 2170 cell, the 4680 cell must have a dual-tab or all-tab design to be viable.

The total heat generation throughout the discharge from current collectors and electrodes for dual-tab and all-tab designs is compared in Fig. 3(e). As the single-tab configuration cannot be discharged at 1.5C, it is not considered here. The current collectors can be seen to act as a

major source of heat generation in the dual-tab 4680, a role they did not play for the 2170 cell (as shown in Fig. 2(d)).

3.2. Power performance

In this section, the pulse power capability for the four cells (2170 single-tab, 2170 all-tab, 4680 dual-tab and 4680 all-tab cells) is investigated, as it is a key figure of merit in applications. The power capability is defined as the maximum discharge power that can be sustained for 10 s while also maintaining the terminal voltage above a cutoff voltage of 3.0 V. Fig. 4(a) shows the power capability when starting from different SoC between 100% and 10%. For all cells, the power capability decreases monotonically with a decrease in starting SoC. The 4680 cell with all-tab design provides the highest power among the four cells for all starting SoC levels. At 100% SoC, the power capability of the 4680 all-tab cell is 543.7 W (corresponding to 6.7C), while the power capability of the 2170 single-tab cell, i.e., the LG M50T cell, is 78.4 W (corresponding to 5.2C). The power capability of the 4680 all-tab cell is 6.9 times that of the 2170 single-tab cell, i.e. the LG M50T cell. The power capability of a 4680 cell is halved when the all-tab design is replaced with dual-tab design, as shown in Fig. 4(a). Dual-tab design causes the lower cutoff voltage to be reached sooner than in the case of all-tab design. The power capacity for 2170 cell single-tab and all-tab
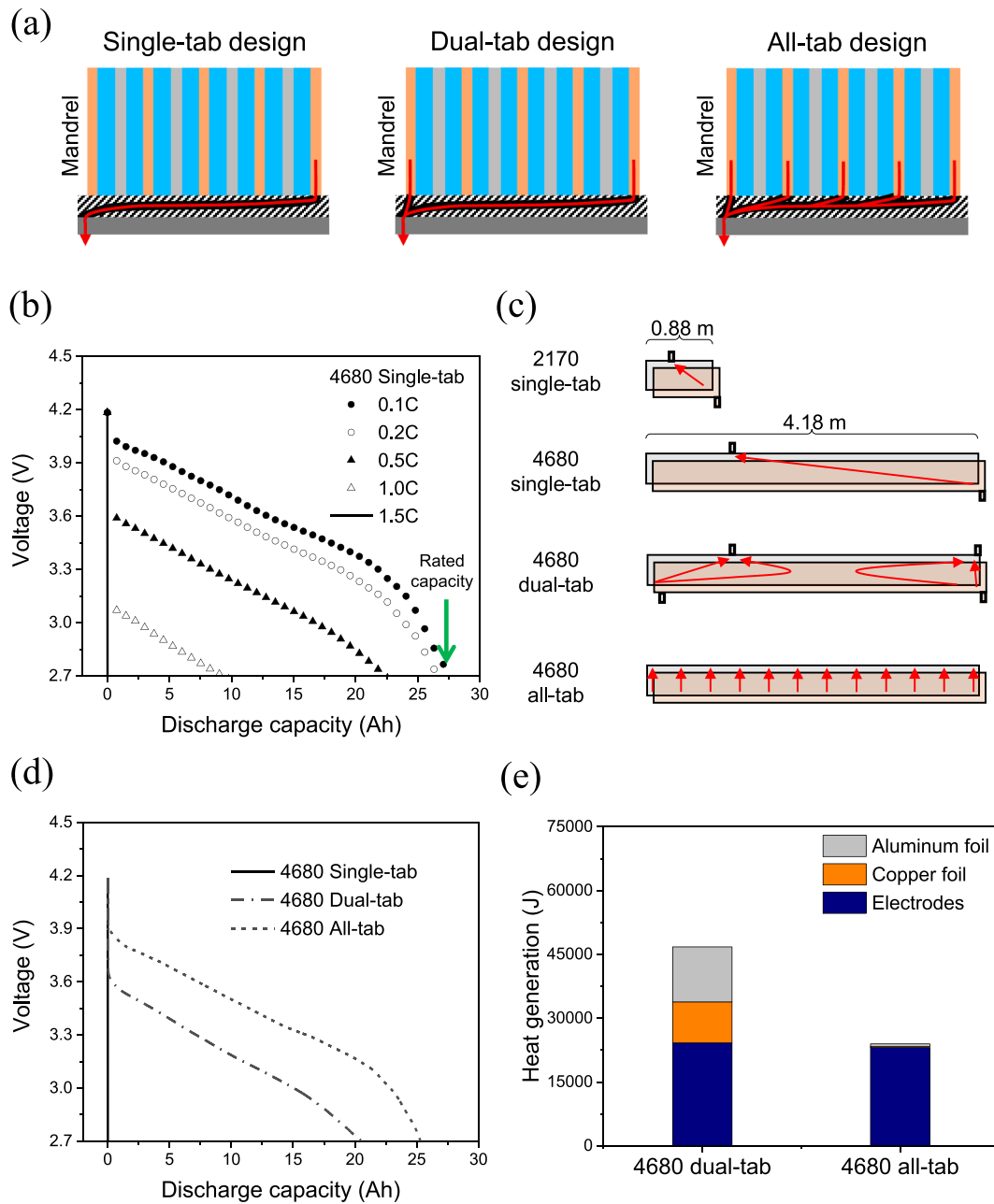
Fig. 3. Comparison of tab designs for a 4680 cylindrical cell during 1.5C discharge under convective thermal boundary condition. (a) Schematic of single-tab, dual-tab and all-tab designs (legend as in Fig. 1). (b) Capacity check for 4680 single-tab cell under different C rates. (c) Schematic of the electrical path through the current collector for single-tab 2170 and 4680 cell, dual-tab and all-tab 4680 cell. (d) Terminal voltage for single-tab, dual-tab and all-tab design. (e) Total heat generation of electrodes and current collectors for dual-tab and all-tab design during discharge.

designs is compared in **Fig. 4**(b) for the appropriate y-axis power range. The all-tab design improves the power for the 2170 cell, but not nearly as significantly as for the 4680 cell (all-tab vs dual-tab design), as the electrical path for a 4680 cell is significantly longer than that for the 2170 cell. The maximum C rate is shown in **Fig. 4**(a) for the four cells. The maximum C rate for the all-tab design is significantly higher than its single-tab/dual-tab counterpart, for both 4680 and 2170 cells. For the same cut-off voltage, the cell with all-tab design allows higher C rate capability in comparison to single-tab/dual-tab design. The C rate capability for all-tab 2170 and all-tab 4680 cell is similar, because the two cells have similar structure in the case where the extra resistances induced by tab configuration are minimized.

4. Benefit from thermal connection

4.1. Model validation for the prediction of the base cooling Cell Cooling Coefficient (CCC) on 2170 cells

An obvious feature of the tabless design is that the contact between the jellyroll and the can at the negative side is made via the copper tabs, instead of via separator layers, with thermal conductivity of 398 Wm^{-1} K^{-1} vs. 0.34 Wm^{-1} K^{-1} [43]. The metal-metal thermal connection makes heat dissipation much more efficient than for a separator-metal connection. The Cell Cooling Coefficient (*CCC*) has shown to be a meaningful metric to quantify the heat generation and rejection ability of a battery cell [22]. In this section, the *CCC* is calculated for the various cells based on virtual experiments run on the 3D distributed ECN model,
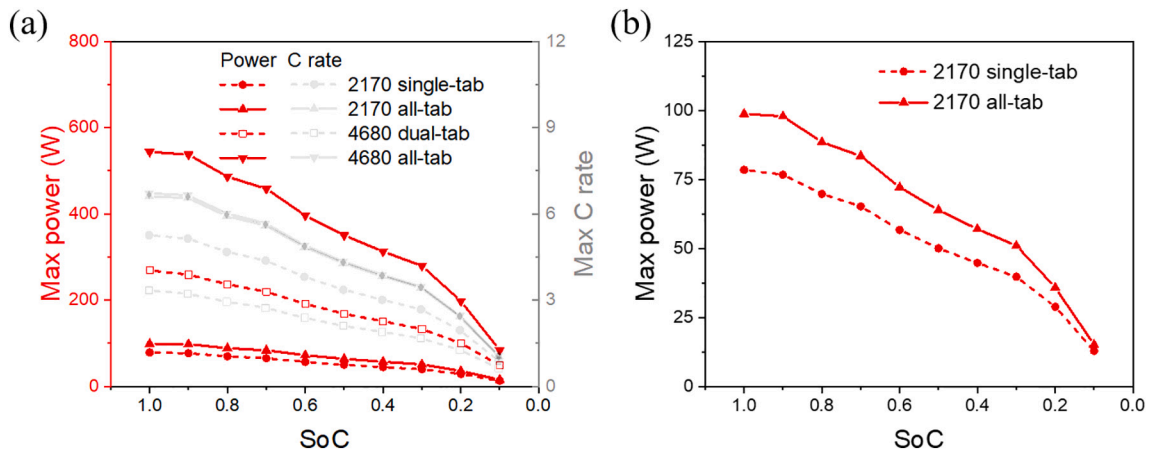
Fig. 4. Power capability for the four cylindrical cells when discharged from different SoC. (a) Maximum capacity and C rate for the 2170 single-tab and all-tab cells, and the 4680 dual-tab and all-tab cells. (b) Zoomed-in maximum power for the 2170 single-tab cell and the 2170 all-tab cell.

and used to compare the heat rejection ability associated with the different tab designs.

The experiments are set up on a base cooled LG M50T for the 2170 cell, yielding a value for CCC_{base}. The experimental rig is designed to restrict all thermal pathways except the one of interest: base cooling path. The cooling path is designed to develop an easily measurable temperature gradient along its length when heat flows from the cell. The experimental setup involves connecting the cell at the top and base with
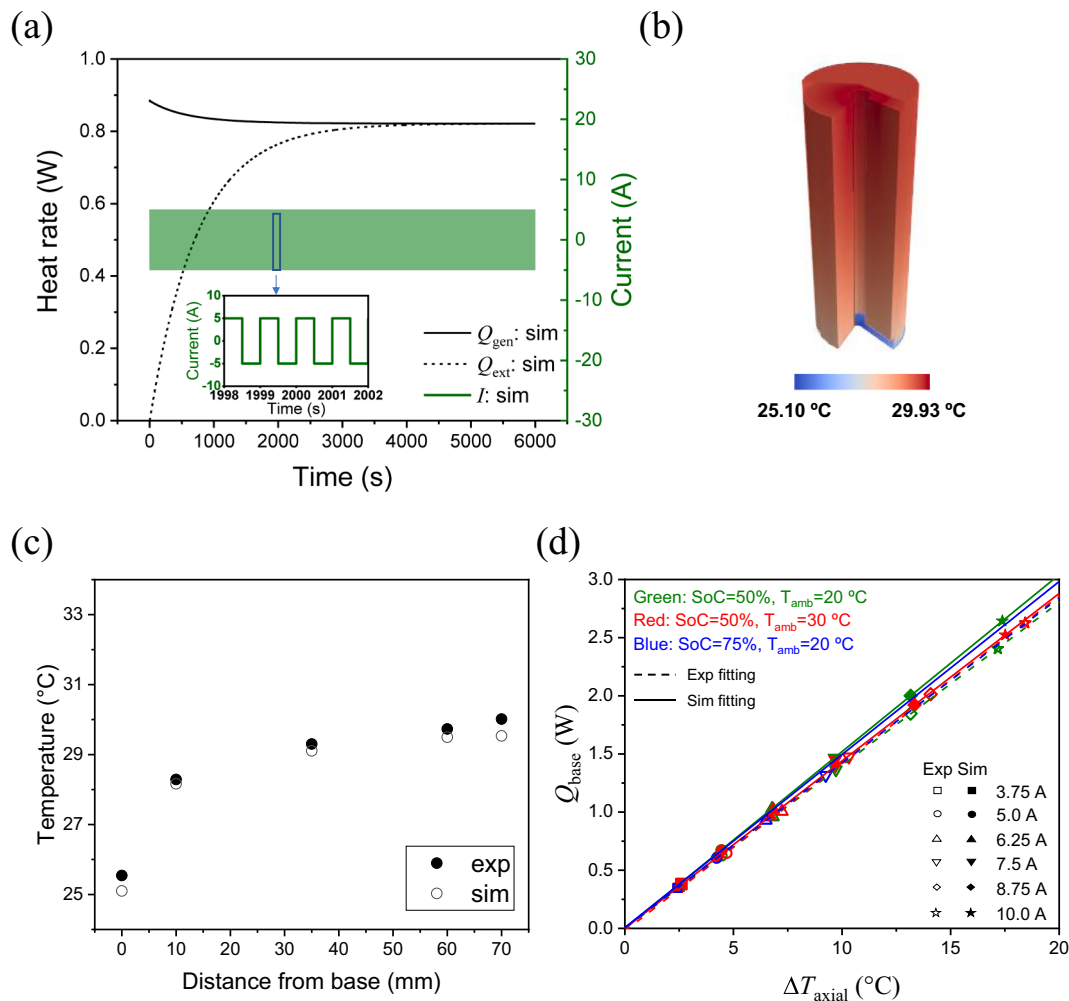

Fig. 5. Model validation results for the *CCC* experiment on 2170 cylindrical LG M50T cell. (a) Model predicted heat rate evolution for a 1C (5A) current during the virtual *CCC* experiment. (b) Predicted temperature distribution throughout the cell at steady state for a 1C (5A) pulsed current. (c) Simulation and experimental data for temperature at different side surface locations along the axial direction of the cell can. (d) Simulation and experimental data for the base cooling rate Q_{base} vs the temperature difference between positive and negative side ΔT_{axial} under different current pulse amplitude, cell SoC and ambient temperature.

spot welded nickel tabs clamped between brass blocks. A tab is spot welded as closely to the edge of the base as possible in order to minimize its effect on the cooling path. The connected cell is encased in insulating foam with only the base of the cell in contact with a Peltier controlled cooling fin. Two main assumptions have been made in calculating the CCC_{base} from the experimental data: 1) that the main heat rejection pathway lies along the cell axial direction and all heat is rejected through the base of the cell, and 2) that the heat generation is all caused by the cell itself, thus ignoring heat generation from the tab weld. More details on the experimental setup can be found in Marzook et al. [24], done on the same cell type LG M50T. In the experiment, a switching discharge/charge current with the frequency of 1 Hz is applied until the cell and rig thermalize. These highly specific conditions are replicated under different discharge/charge rates (0.25C, 0.5C, 0.75C. 1C, 1.25C, 1.5C, 1.75C and 2C), different temperature (20 °C and 30 °C) and initial SoC (50% and 75%).

For the model setup, the same pulsing current is applied as in the experiment, as shown in the inset of Fig. 5(a). The base surface is set as the cooling area. The thermal boundary condition for the side surface and the positive cap surface is assumed to be characterized by a small heat transfer coefficient h_{insu} to account for the small heat loss through the insulation layer surrounding those surfaces and down the tabs connecting the cell electrically. The effective thermal conductivity between the jellyroll base and the metal can, λ_{link}, is set as a small value in the model to represent the weak heat transfer through one tab and separator layers. The values of $h_{insu} = 3.5\ Wm^{-2}\ K^{-1}$ and $\lambda_{link} = 2.6\ Wm^{-1}\ K^{-1}$ are found to allow the model predicted temperature and heat transfer rate to match the measured values.

Under these conditions, most of the extracted heat is transferred through the cell base. The heat extraction rate Q_{ext} and the heat generation rate Q_{gen} predicted by the model are shown in Fig. 5(a). Initially, the heat generation rate decreases and the heat extraction rate increases. This behavior is caused by the increasing cell temperature. The resistance decreases with temperature for the LG M50T cell [13], thus lowering the heat generation rate Q_{gen}, which is governed by irreversible losses. The heat extraction rate Q_{ext}, on the other hand, is proportional to the difference between the internal cell temperature at the cell base and the external cooling temperature of the cooling plate. This difference increases as the internal cell temperature increases. Around 3500 s, the heat extraction rate Q_{ext} and the heat generation rate Q_{gen} balance, as the system reaches steady state and the CCC_{base} can be calculated. The model-predicted temperature distribution inside the cell during steady state reached for a 1C (5 A) current is shown in Fig. 5(b). The thermal gradient forms mostly along the axial direction, reaching a temperature difference $\Delta T_{axial} = 4.83°C$ between the top and bottom of the cell can. The measured and predicted temperatures at steady state along the axial direction are compared in Fig. 5(c). The base cooling CCC_{base} [W K^{-1}] of this LG M50T cell is given as:

$$CCC_{base} = \frac{Q_{base}}{\Delta T_{axial}}, \quad (1)$$

where Q_{base} [W] is the heat rejection rate through the cell base [22]. Q_{base} is a main contributor to Q_{ext}, alongside the heat flow rate through the side and top surfaces of the can. The experimental and simulation results for the temperature difference ΔT_{axial} and the base cooling rate Q_{base} are in good agreement, as shown in Fig. 5(d) for different pulsing currents, SoCs and ambient temperature conditions. Under these pulsing currents, the CCC is around 0.14 W K^{-1} for both model prediction and experimental measurement.

4.2. Predicted base and side Cell Cooling Coefficient (CCC) for 4680 cells

The cylindrical cell model validated for CCC_{base} of a 2170 cell is used to predict the ability of the 4680 cell to be cooled, by calculating base cooling CCC_{base} and side cooling CCC_{side}. The metal-metal thermal

configuration for the tabless cell, shown in Fig. 1(e), is expected to improve the rate of heat rejection through the cell base. The benefit of improved thermal connection by the tabless connection is quantified by comparing the different options for internal thermal connection between the jellyroll base and the metal can base.

For the all-tab scenario, the thermal connection between jellyroll base and metal can base at the negative side of the cell is set to be the same as that found in the 2170 LG M50T cell, i.e., the same value is assumed for the effective thermal conductivity λ_{link} for the connection between jellyroll base and metal can. For the tabless scenario, it is assumed that the copper foil of the tabs and the metal can are in perfect thermal contact with each other at the negative terminal. The other thermal connections, such as that between the positive current collector and the can, as well as that between the electrodes and the can, remain unchanged from the separator-can thermal contact scenario, i.e., with thermal conductivity $\lambda_{link} = 2.6\ Wm^{-1}K^{-1}$. An equivalent setup is simulated on the positive connection, where the aluminum foil and the metal can are assumed to be in perfect thermal contact.

In the CCC simulation test, pulses of 1.5C discharge and 1.5C charge are applied to three cells: 2170 single-tab (LG M50T cell as reference, separator-metal connection between jellyroll and can), 4680 all-tab (separator-metal thermal connection) and 4680 tabless (metal-metal thermal connection). To account for the effects of cell size, a geometry-normalized CCC value is calculated, as introduced by Marzook et al. for cylindrical cells [24]. The nomalized $\widetilde{CCC}_{base}^{GN}$ [W K^{-1} m^{-3}] is calculated from the temperature gradient across the height of the cell $\Delta T_{axial}/L$ and the base cooling rate per area of the base Q_{base}/A_{base}:

$$\widetilde{CCC}_{base}^{GN} = \frac{Q_{base}/A_{base}}{\Delta T_{axial}/L} = \frac{CCC_{base}}{A_{base}/L}, \quad (2)$$

where L [m] is the cell height and A_{base} [m^2] is the cell base area. The predicted temperature gradient $\Delta T_{axial}/L$ and base cooling rate per area Q_{base}/A_{base} at steady state for the three cells are compared in Fig. 6(a). The full parameters of the model is listed in Table 2. The base cooling heat extraction rates Q_{base}/A_{base} are similar for the three cells, while the thermal gradients vary significantly. The 4680 tabless cell experiences nearly half the axial thermal gradient of the 2170 and 4680 all-tab cells. The metal-metal contact enables efficient heat transfer in the tabless cell, while the separator-metal contact in the single tab and all tab cells forms a thermal bottleneck.

The CCC results are shown in Fig. 6(b). The normalized $\widetilde{CCC}_{base}^{GN}$ for 4680 all-tab cell is similar to that of the 2170 cell. The tabless design in the 4680 cell yields the highest $\widetilde{CCC}_{base}^{GN}$ among the three cells, by a factor of two. The value of CCC_{base} (i.e. before considering the effect of cell geometry) for the 4680 tabless cell is 1.15 WK^{-1}. This value is higher than the value corresponding to traditionally better cooling scenarios, such as surface-cooled pouch cells, that have been found to have CCC values ranging within 0.99 WK^{-1} for a commercial pouch cell [22].

An alternative comparison can be made by normalizing CCC with respect to the heat generation rate, $q = (CR \cdot Q)^2 \cdot R$, where CR is the C rate, Q [Ah] is the cell rated capacity and R [Ω] is the cell resistance. The CCC normalized for heat generation $\widetilde{CCC}_{base}^{HG}$ [W K^{-1} Ah^{-2} Ω^{-1}] can be approximated as:

$$\widetilde{CCC}_{base}^{HG} = \frac{CCC_{base}}{Q^2 \cdot R_0}, \quad (3)$$

where R_0 [Ω] is the instantaneous ohmic resistance obtained independently from the simulated instantaneous voltage drop under an applied current of 1.5C at 25 °C from 50% SoC. The value of R_0 for the 2170 single-tab cell, the 4680 all-tab cell and the 4680 tabless cell are found to be $3.71 \times 10^{-2}\ \Omega$, $5.14 \times 10^{-3}\ \Omega$ and $4.88 \times 10^{-3}\ \Omega$, respectively. With these values, the $\widetilde{CCC}_{base}^{HG}$ for 4680 tabless cell is the highest among these three cells (almost twice of the non-tabless 2170 single-tab and 4680 all-
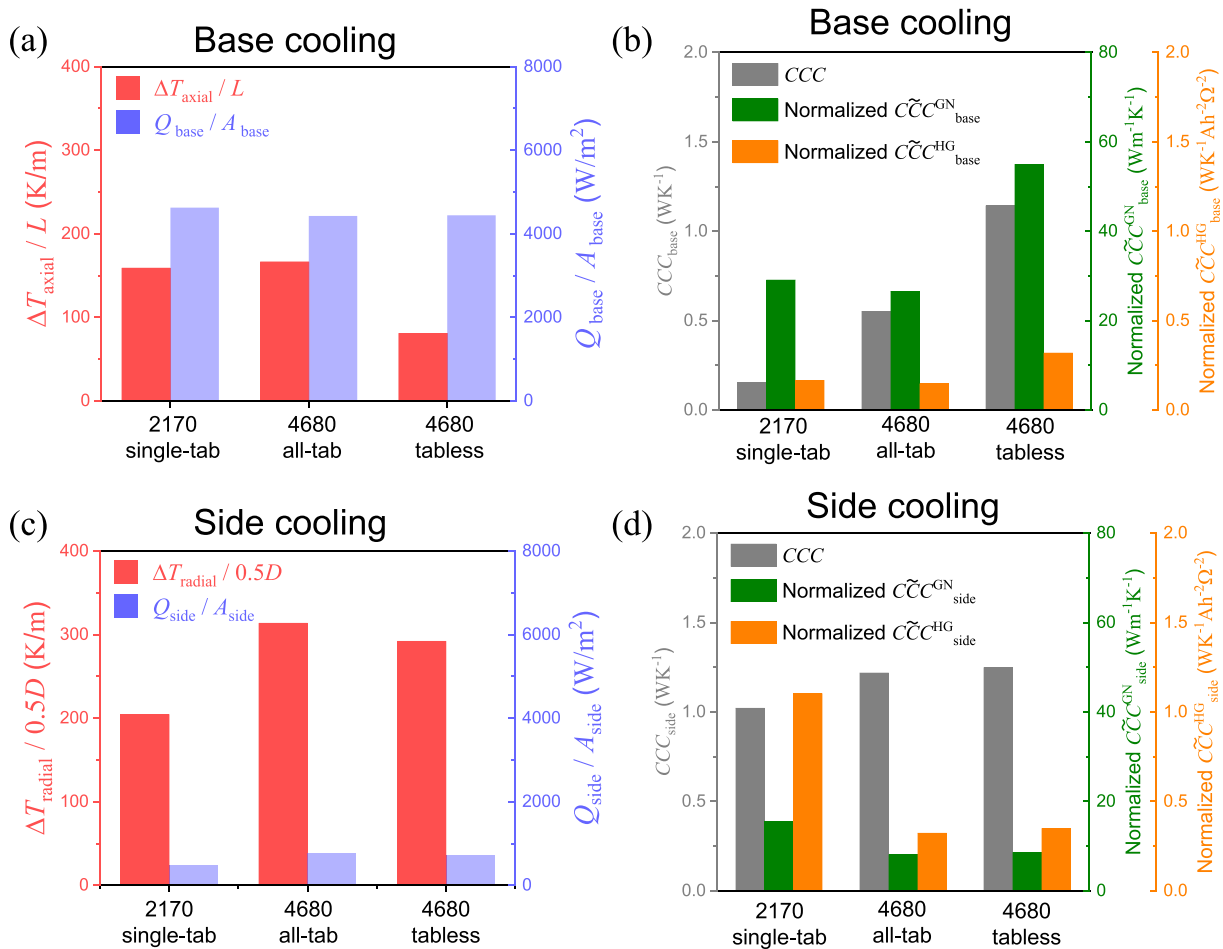
Fig. 6. Simulated base and side cooling *CCC* results for 2170 single-tab, 4680 all-tab and 4680 tabless cells. (a) Cell temperature gradient along the height of the cell and heat rejection rate per area from the cell base. (b) Base cooling CCC_{base} and normalized $C\widetilde{C}C^{GN}_{base}$ and $C\widetilde{C}C^{HG}_{base}$. (c) Cell temperature gradient along the radial direction and the heat rejection rate per area from the cell side surface. (d) Side cooling CCC_{side} and normalized $C\widetilde{C}C^{GN}_{side}$ and $C\widetilde{C}C^{HG}_{side}$.

Table 2
Parameters of the model for base cooling and side cooling CCC.

	2170 single-tab	4680 all-tab	4680 tabless
A_{base} (mm^2)	346.36	1661.90	1661.90
A_{side} (mm^2)	4618.14	11,561.05	11,561.05
L (mm)	70	80	80
D (mm)	21	46	46
ΔT_{axial} (°C)	11.12	13.30	6.46
Base Q_{gen} (W)	2.06	8.36	8.01
Base Q_{ext} (W)	2.06	8.36	8.01
Q_{base} (W)	1.60	7.35	7.38
ΔT_{radial} (°C)	2.15	7.21	6.71
Side Q_{gen} (W)	2.19	8.83	8.42
Side Q_{ext} (W)	2.19	8.83	8.42
Q_{side} (W)	2.19	8.79	8.38

tab cells), showing superior thermal performance, as shown in **Fig. 6**(b).

Some applications employ partial surface cooling as their thermal management approach. For this reason, the analysis above is repeated for three cylindrical cells under surface cooling. In this reference case, the entire surface is cooled. The side cooling CCC_{side} [W K^{-1}] is defined as:

$$CCC_{side} = \frac{Q_{side}}{\Delta T_{radial}}, \qquad (4)$$

where Q_{side} [W] is the heat rejection rate through the cell side surface, and ΔT_{radial} is the temperature difference between the core and the side

surface at the cell height mid-point. This definition is analogous to that of surface cooling for pouch cells, and corresponds to a theoretical measure, enabled by the model, of a cylindrical cell's ability to be cooled through its side surface. Of course, in experiments the core temperature is not easily available. The side cooling normalized for geometry $C\widetilde{C}C^{GN}_{side}$ [W K^{-1} m^{-3}] is calculated from the temperature gradient $\Delta T_{radial}/0.5D$ and the base cooling rate per area Q_{base}/A_{base}, where D [m] is the cell diameter:

$$C\widetilde{C}C^{GN}_{side} = \frac{Q_{side}/A_{side}}{\Delta T_{radial}/0.5D} = \frac{CCC_{side}}{A_{side}/0.5D}, \qquad (5)$$

here A_{side} [m^2] is the surface area of the side of the cell. The *CCC* normalized for heat generation $C\widetilde{C}C^{HG}_{base}$ is:

$$C\widetilde{C}C^{HG}_{side} = \frac{CCC_{side}}{Q^2 \cdot R_0}, \qquad (6)$$

where R_0 is calculated at 50% SoC under 25 °C initial temperatures. The predicted temperature gradient $\Delta T_{radial}/0.5D$ and the side cooling rate per area Q_{side}/A_{side} at steady state for the three cells are compared in **Fig. 6**(c). The full parameters of the model are listed in Table 2. The thermal gradient along the radial direction for the 4680 cell is higher than that of 2170 single-tab cell, because of the larger radial dimension, and thus longer heat path, along an axis with relatively poor thermal conductivity. The side cooling *CCC* results are shown in **Fig. 6**(d). The normalized $C\widetilde{C}C^{GN}_{side}$ and $C\widetilde{C}C^{HG}_{side}$ for the 4680 cell (all-tab and tabless) are significantly lower than those of the 2170 cell, in stark contrast to the

base cooling results in Fig. 6(b). The side cooling surface-to-volume ratio is inversely proportional to the cell radius, while base cooling surface-to-volume ratio is independent of radius. Therefore, for side cooling, the tabless design does not improve the heat rejection, while the drawback of the larger radius impacts the heat rejection from the core of the 4680 cell.

4.3. Average temperature and thermal gradients predicted for 4680 cells under normal discharge condition

Beyond *CCC*, the viability of cells can be quantitatively analyzed based on the average temperature and temperature gradients they are expected to experience during operation [13]. The effect of the thermal connection on the transient temperature performance (volume-averaged temperature and thermal gradients) of the 4680 cell is investigated for a 1.5C discharge base cooled by a cooling plate at 25 °C and with side surfaces thermally insulated.

The volume-averaged temperature for the 4680 all-tab cell and tabless cell are shown in Fig. 7(a). For the 4680 all-tab cell, the volume-averaged temperature rise is the highest, reaching 48 °C at the end of discharge. In contrast, the cell with tabless design has a significantly lower volume-averaged temperature, around 35 °C at the end of discharge. It is expected that a cell with a lower average temperature will degrade slower. The presence and magnitude of thermal gradients is also expected to be strongly correlated to reduced performance and lifetime. The temperature difference ΔT (i.e. the difference between maximum T_{max} and minimum temperature T_{min} anywhere within the cell) is shown in Fig. 7(b). The thermal gradient for the all-tab design is twice the value of tabless design, indicating that the all-tab cell does not benefit from base cooling as much as the tabless cell. The temperature distribution at the end of discharge is shown in Fig. 7(c). The

temperature difference between the jellyroll and the metal can at the negative side is significant for the all-tab cell, indicating a thermal bottleneck created by the poor thermal connection pathway, unlike in the tabless cell.

Since base cooling has been shown to be very efficient for a tabless cell, the potential gains that can be achieved by top and base cooling are explored. As shown in Fig. 7, the average cell temperature and the temperature difference can be further decreased by cooling both top and base, in comparison to base-only cooling. However, there are obvious practical hindrances to cooling the top due to the presence of electrical connections and venting points.

4.4. Choosing the best thermal management for the 4680 tabless cell

Using the model developed, two common cooling schemes, top/base cooling and side cooling, are applied on a 4680 tabless cell, in order to evaluate their effect on its thermal performance. All other surfaces are assumed insulated, to somewhat mimic the conditions within a pack, when the cell is surrounded by other heat-generating cells. Convective boundary conditions are used to retrieve the effect of forced air cooling, while conductive boundary conditions are used to retrieve the effect of contact plate cooling. In convective cooling, a heat transfer coefficient of 30 $Wm^{-2} K^{-1}$ and an ambient temperature of 25 °C are assumed. In conductive cooling, the temperature on the cooling surface is fixed at 25 °C.

The simulated volume-averaged temperature for the four cooling schemes considered is shown in Fig. 8(a). The conductive cooling scenarios lead to significantly lower volume-averaged cell temperature than the convection scenarios, due to the higher heat transfer rate between the cell and its ambient enabled by the metal-metal conduction than the metal-air convection boundary condition. However, side
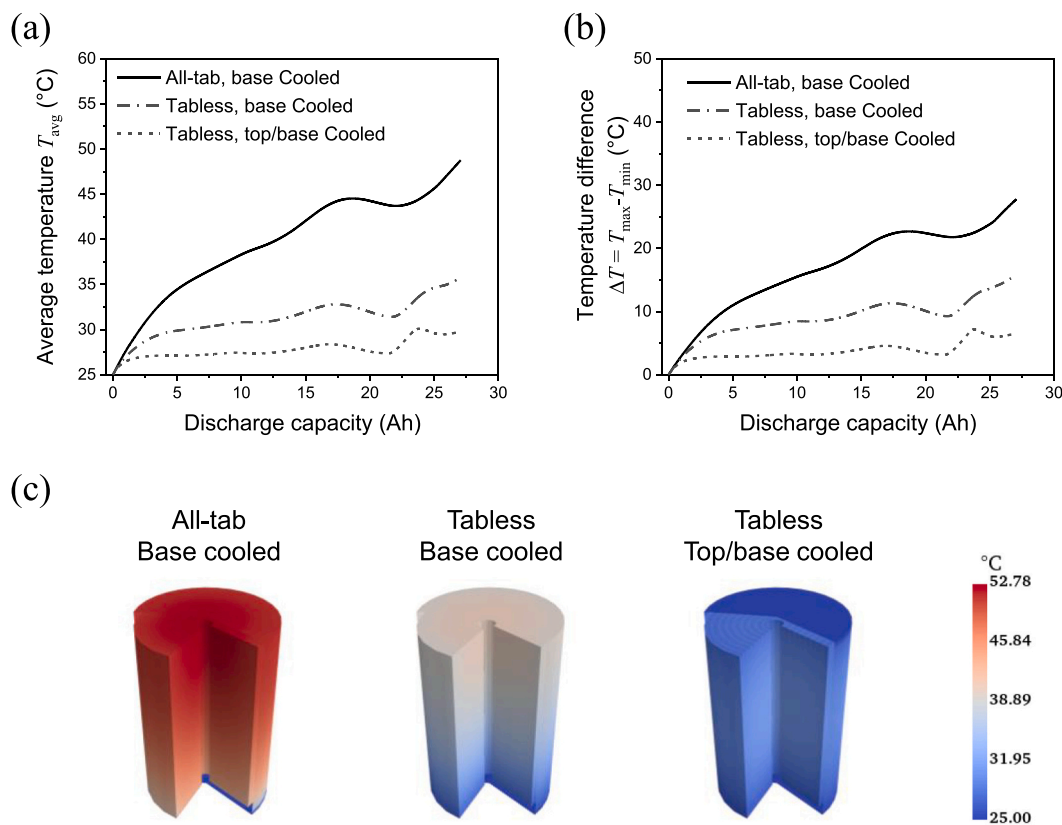

Fig. 7. Thermal performance for 4680 all-tab and tabless cells during a 1.5C discharge for base cooling and top & base cooling with a plate temperature of 25 °C and side surfaces insulated. (a) Volume-averaged temperature and (b) temperature difference across the cell. (c) Temperature distribution at end of discharge (after 2400 s of discharge time).
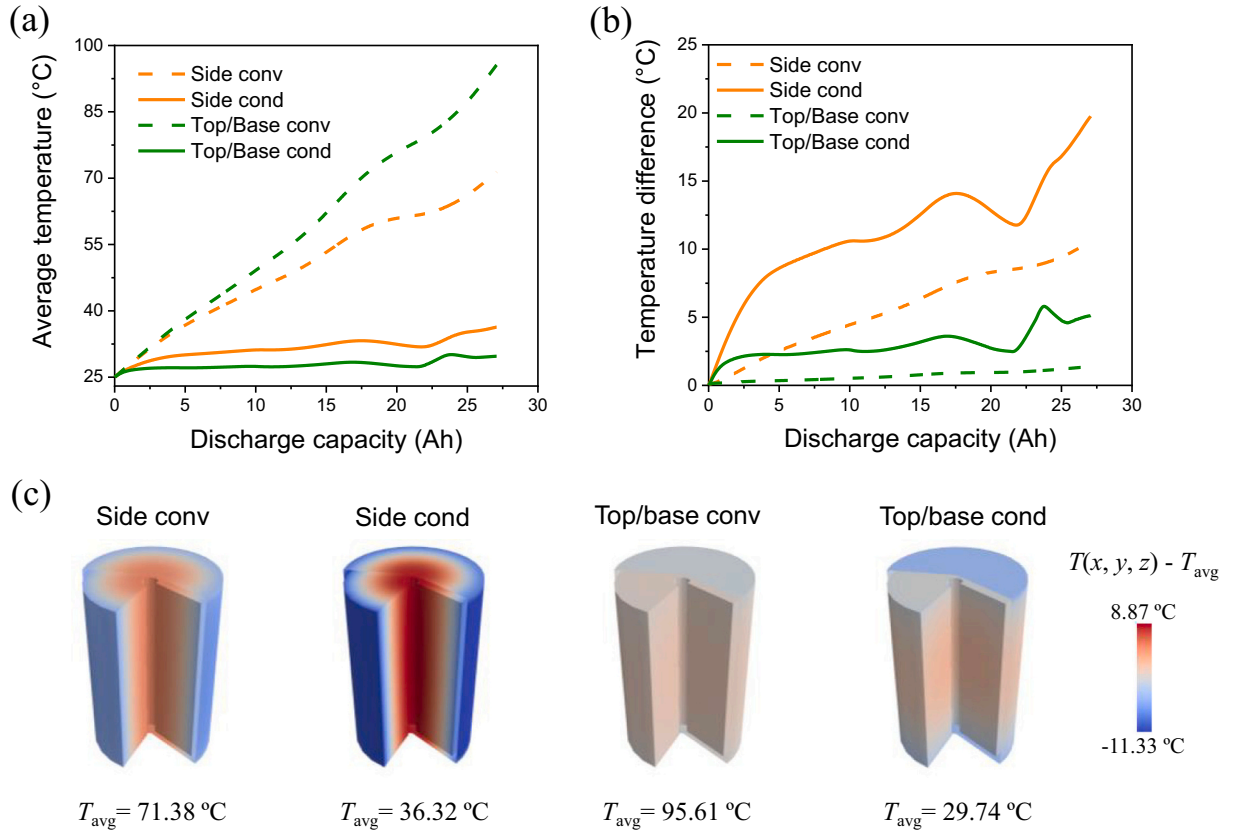
Fig. 8. Model predictions of the thermal performance of a 4680 tabless cell during a 1.5C discharge under four thermal management conditions: side convection, side conduction, top/base convection and top/base conduction. (a) Volume-averaged temperature and (b) the maximum temperature difference within the cell. (c) Internal temperature distribution at the end of discharge.

conductive cooling causes the largest temperature difference across the cell, as shown in **Fig. 8**(b). This high level of temperature difference is guaranteed to cause accelerated degradation [11]. Although the temperature difference for top/base convection is the lowest, this may not the best cooling choice for long cycle life, since the volume-averaged temperature is relatively high, as shown in **Fig. 8**(a). The temperature distribution for the 4680 cell under the four cooling scenarios at the end of discharge is shown in **Fig. 8**(c). The thermal gradient within the cell forms along the radial direction for side cooling and mainly along the axial direction for top/base cooling scenarios, for both convection and conduction. Considering the smaller average temperature and thermal gradient, it can be concluded that top/base conductive cooling is the best cooling scheme for the 4680 tabless cell. In contrast, the best cooling approach for the 2170 cell was found to be side cooling [13], due to the larger cooling area of the side surface than the top/base surface.

5. Discussion

The thermal performances of the 4680 tabless cell and the 2170 single-tab cell are analyzed in this section based on the virtual model experiments run so far. In comparison to the 2170 cell, the 4680 cell is disadvantaged by geometry: 1) the 4680 cell has lower surface-to-volume ratio for side cooling, and 2) the longer radius of 4680 cell can lead to higher radial thermal gradients. In both cases, a tabless design has been demonstrated to improve the thermal performance. Therefore, a comparison between the 2170 cell and 4680 cell is not straightforward and must be conducted separately for each of the different cooling scenarios of interest.

In order to compare the different cells, tab configurations, and thermal management options, we have used the 'average functions' defined in our previous work [13]. As described by Li et al. [13], ΔT_{avg}

measures the ability of the cell to maintain the cell internal average temperature close to a target value T_{target}, time-averaged over the discharge process. ΔT_{avg} is given by:

$$\Delta T_{avg} = \frac{S_1}{t} = \frac{1}{t} \int_0^t \left(T_{avg}(t) - T_{target} \right) \cdot dt, \tag{7}$$

where S_1 is the integral of the temperature over time t. T_{target} is set here as 25 °C, to match the ambient and cooling plate temperature. The second metric ΔT_{grad} measures the emerging thermal gradient within the cell, time-averaged over the discharge process. ΔT_{grad} is given as:

$$\Delta T_{grad} = \frac{S_2}{t} = \frac{1}{t} \int_0^t \left(T_{max}(t) - T_{min}(t) \right) \cdot dt, \tag{8}$$

where S_2 is the integral of the temperature difference over time t. T_{max} and T_{min} are the maximum and minimum temperatures in the jellyroll, respectively. For better thermal performance, a cell has as small a value as possible for both metrics.

These two metrics, ΔT_{avg} and ΔT_{grad}, are calculated for the conditions explored so far: 1.5C constant current discharge, with 25 °C ambient and cooling plate temperature, under conductive cooling of top & base and side, and under convective cooling at top & base and side, characterized by 30 Wm^{-2}K^{-1}, with all other surfaces insulated. The results for the 2170 and 4680 cells are plotted in Fig. 9 and quantitatively compared in Table 3. When the 4680 cell is cooled from the top and base by convection or conduction, both ΔT_{avg} and ΔT_{grad} are significantly lower than those for the 2170 cell under the same conditions, as listed in Table 3. The best thermal performance of the 4680 cell ($\Delta T_{avg} = 5.62°C$, $\Delta T_{grad} = 7.61°C$) is similar to the best thermal performance of the 2170 cell ($\Delta T_{avg} = 4.81°C$, $\Delta T_{grad} = 8.23°C$). The former is achieved under top and base conduction cooling, while the latter under side conduction
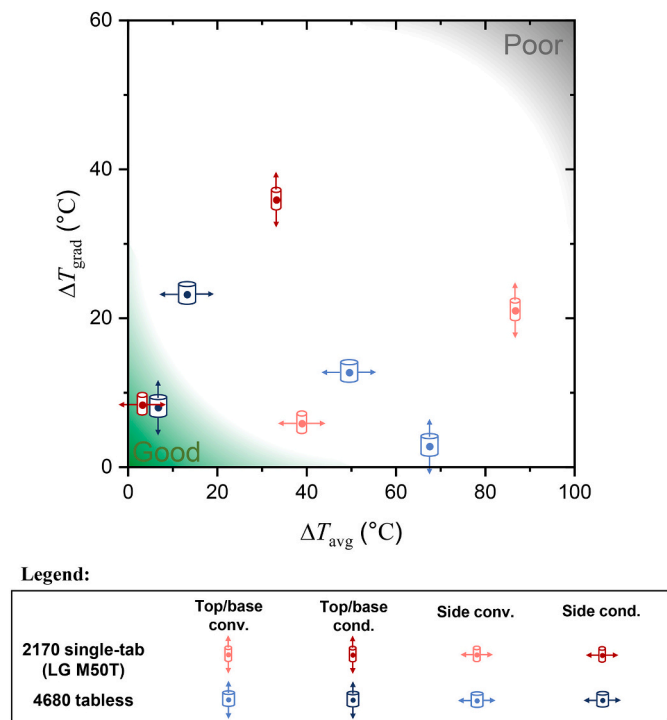
Fig. 9. Predicted thermal performance of the 2170 cell and the 4680 cell under top/base cooling and side cooling approaches. The 2170 cell side conduction cooling and the 4680 cell top/base conduction cooling performance are very similar, indicating the optimum cooling approaches for these cells.

Table 3
Thermal metric values (ΔT_{avg} | ΔT_{grad}, unit: °C) for the 2170 and the 4680 cells under top/base and side cooling, as plotted in **Fig. 9**.

	Top/base conv.	Top/base cond.	Side conv.	Side cond.
2170 single-tab	86.84 | 20.92	33.33 | 35.66	39.07 | 5.66	4.81 | 8.23
4680 tabless	67.77 | 2.64	5.62 | 7.61	49.74 | 12.44	13.23 | 23.02

cooling. This result demonstrates there may not need to be a trade-off between achieving high energy density and good thermal performance, as long as cylindrical cells can be built with a tabless design. Under side cooling, the 2170 cell performs close to the 4680 cell with respect to both ΔT_{avg} and ΔT_{grad}. For the 4680 cell, the best cooling approach is conductive top/base cooling; for the 2170 cell, it is side conductive cooling, as it does not generate a high internal thermal gradient. The surface-to-volume ratio for the 2170 cell is roughly double that of the 4680 cell, 2.19×10^2 m^{-1} and 1.12×10^2 m^{-1} respectively. The high surface-to-volume ratio of the 2170 cell maximizes the heat extraction efficiency and maintains a low volume-averaged temperature. The relatively smaller radius of the 2170 cell enables it to avoid high thermal gradients, which do occur in the 4680 cell, as listed in in Table 3: for side convection the 4680 cell has a thermal gradient higher by roughly a factor of two, while for side conduction by roughly a factor of three.

As an immediate implication to battery engineering, the two metrics ΔT_{avg} and ΔT_{grad} should lead the cell selection process, itself an important process for both the stationery energy storage system (ESS) and the electric vehicle (EV) industries. We recommend that the best cell is selected as the one that has lowest values for the two characteristics, as calculated from an appropriate model. If practical, a tabless design is shown to lead to better performance when other parameters, such as cell

dimension and cooling approach, remain unchanged. Once the cell is selected, the cooling system should be designed according to the condition that minimizes the two metrics. In this manner, the combination of chosen cell design and thermal management will maximize the cell performance and thus extend the battery system lifetime.

6. Conclusions

A distributed 3D coupled electro-thermal equivalent circuit network (ECN) model of cylindrical lithium-ion batteries is used to study the effect of cell design and cooling approach on performance. Multiple tab configurations and thermal management approaches are considered for 2170 and 4680 cells. The distributed ECN model includes the non-active components, with particular attention to correctly describing the thermal paths within the cell. The internal thermal connection between the jellyroll and the metal can is found to be essential in determining the performance of the cell, despite it being ignored in most published battery modelling studies.

The model was validated against base cooling cell cooling coefficient (*CCC*) experimental tests under various SoC, current and temperature conditions on a 2170 single tab cell, the LG M50T. Once validated, the model was used to explore the capabilities of a tabless large form factor 4680 cylindrical cell, for example as the one developed by Tesla. The simulation results show that the tabless design significantly improves both the electrical and thermal performance of a cylindrical cell. Using base cooling, the normalized cell cooling coefficient for the 4680 tabless cell is almost twice that of the non-tabless 2170 single-tab and of the 4680 all-tab cells. This improvement is found to be caused by the shortened electrical path and the enhanced internal metal-metal thermal connection between the jellyroll and the metal can, at both the negative and positive terminals. The results also show that a 4680, or other large format cylindrical cell, would not be viable without a tabless design, as they would either reach the voltage cut-off too early due to high resistances, or overheat.

A procedure for finding the best thermal management for cylindrical cells is proposed by defining two thermal metrics. For the 4680 tabless cell compared to the 2170 cell, the thermal metrics of average temperature and internal thermal gradient are found to be no worse, while the 4680 tabless tab cell has 5.4 times the energy and 6.9 times the power. The results show that the best cooling strategy for the single-tab 2170 is side cooling, while for the 4680 tabless cell it is base cooling. The optimum cooling strategy is strongly affected by both the surface-to-volume ratio and the internal thermal connection of the cell. The surface-to-volume ratio dominates for the single-tab 2170, leading to side cooling, while the enhanced thermal connection between the jellyroll and metal can dominates for the 4680 tabless cell leading to base cooling.

The study unveils that the ability to manufacture with a continuous (or tabless) tab configuration is essential to creating viable large form factor cylindrical cells. Importantly, this is one example of significant advances in cell design from a thermal management point of view, creating a net positive impact on cell performance, despite increasing the mass of the cell. This demonstrates there does not need to be a trade-off between cell size and thermal performance, as long as cylindrical cells are designed tabless.

CRediT authorship contribution statement

Shen Li: Conceptualization, Data curation, Formal analysis, Investigation, Methodology, Software, Validation, Visualization, Writing – original draft, Writing – review & editing. **Mohamed Waseem Marzook:** Data curation, Formal analysis, Investigation, Methodology, Writing – original draft. **Cheng Zhang:** Formal analysis, Methodology, Writing – original draft. **Gregory J. Offer:** Funding acquisition, Supervision, Writing – original draft. **Monica Marinescu:** Conceptualization, Formal analysis, Funding acquisition, Methodology, Supervision,

Writing – original draft, Writing – review & editing.

Declaration of Competing Interest

The authors declare that they have no known competing financial interests or personal relationships that could have appeared to influence the work reported in this paper.

Data availability

Data will be made available on request.

Acknowledgements

References

[1] Global EV Outlook. 2020. https://doi.org/10.1787/d394399e-en [Accessed 11 June 2023].

[2] Ouyang M, Feng X, Han X, Lu L, Li Z, He X. A dynamic capacity degradation model and its applications considering varying load for a large format Li-ion battery. Appl. Energy 2016;165:48–59. https://doi.org/10.1016/j.apenergy.2015.12.063.

[3] Hou M, Hu Y, Zhang J, Cao H, Wang Z. Development of electrochemical-thermal modelling for large-format Li-ion battery. Electrochim. Acta 2020;347:136280. https://doi.org/10.1016/j.electacta.2020.136280.

[4] Feng X, Weng C, Ouyang M, Sun J. Online internal short circuit detection for a large format lithium ion battery. Appl. Energy 2016;161:168–80. https://doi.org/10.1016/j.apenergy.2015.10.019.

[5] Klein M, Tong S, Park JW. In-plane nonuniform temperature effects on the performance of a large-format lithium-ion pouch cell. Appl. Energy 2016;165:639–47. https://doi.org/10.1016/j.apenergy.2015.11.090.

[6] Coleman B, Ostanek J, Heinzel J. Reducing cell-to-cell spacing for large-format lithium ion battery modules with aluminum or PCM heat sinks under failure conditions. Appl. Energy 2016;180:14–26. https://doi.org/10.1016/j.apenergy.2016.07.094.

[7] Ye Y, Saw LH, Shi Y, Somasundaram K, Tay AAO. Effect of thermal contact resistances on fast charging of large format lithium ion batteries. Electrochim. Acta 2014;134:327–37. https://doi.org/10.1016/j.electacta.2014.04.134.

[8] Hua X, Heckel C, Modrow N, Zhang C, Hales A, Holloway J, et al. The prismatic surface cell cooling coefficient: a novel cell design optimisation tool & thermal parameterization method for a 3D discretised electro-thermal equivalent-circuit model. ETransportation 2021;7:100099. https://doi.org/10.1016/j.etran.2020.100099.

[9] Feng X, Fang M, He X, Ouyang M, Lu L, Wang H, et al. Thermal runaway features of large format prismatic lithium ion battery using extended volume accelerating rate calorimetry. J. Power Sources 2014;255:294–301. https://doi.org/10.1016/j.jpowsour.2014.01.005.

[10] Grandjean T, Barai A, Hosseinzadeh E, Guo Y, McGordon A, Marco J. Large format lithium ion pouch cell full thermal characterisation for improved electric vehicle thermal management. J. Power Sources 2017;359:215–25. https://doi.org/10.1016/j.jpowsour.2017.05.016.

[11] Hunt IA, Zhao Y, Patel Y, Offer J. Surface cooling causes accelerated degradation compared to tab cooling for lithium-ion pouch cells. J. Electrochem. Soc. 2016;163:A1846–52. https://doi.org/10.1149/2.0361609jes.

[12] Hales A, Diaz LB, Marzook MW, Patel Y, Offer G. The cell cooling coefficient : a standard to define heat rejection from lithium-ion batteries166; 2019. p. 2383–95. https://doi.org/10.1149/2.0191912jes.

[13] Li S, Kirkaldy N, Zhang C, Gopalakrishnan K, Amietszjew T, Bravo Diaz L, et al. Optimal cell tab design and cooling strategy for cylindrical lithium-ion batteries. J. Power Sources 2021;492:229594. https://doi.org/10.1016/j.jpowsour.2021.229594.

[14] Lee KJ, Smith K, Pesaran A, Kim GH. Three dimensional thermal-, electrical-, and electrochemical-coupled model for cylindrical wound large format lithium-ion batteries. J. Power Sources 2013;241:20–32. https://doi.org/10.1016/j.jpowsour.2013.03.007.

[15] Waldmann T, Geramifard G, Wohlfahrt-Mehrens M. Influence of current collecting tab design on thermal and electrochemical performance of cylindrical lithium-ion cells during high current discharge. J Energy Storage 2016;5:163–8. https://doi.org/10.1016/j.est.2015.12.007.

[16] Yao XY, Pecht MG. Tab design and failures in cylindrical li-ion batteries. IEEE Access 2019;7:24082–95. https://doi.org/10.1109/ACCESS.2019.2899793.

[17] Tsuruta K, Dermer ME, Dhiman R. Cell with a tabless electrode, 16/673464. https://patents.google.com/patent/US20200144676A1/en/; 2020.

[18] Tranter TG, Timms R, Shearing PR, Brett DJL. Communication—prediction of thermal issues for larger format 4680 cylindrical cells and their mitigation with enhanced current collection. J. Electrochem. Soc. 2020;167:160544. https://doi.org/10.1149/1945-7111/abd44f.

[19] Worwood D, Kellner Q, Wojtala M, Widanage WD, McGlen R, Greenwood D, et al. A new approach to the internal thermal management of cylindrical battery cells for automotive applications. J. Power Sources 2017;346:151–66. https://doi.org/10.1016/j.jpowsour.2017.02.023.

[20] Sturm J, Rheinfeld A, Zilberman I, Spingler FB, Kosch S, Frie F, et al. Modeling and simulation of inhomogeneities in a 18650 nickel-rich , silicon- graphite lithium-ion cell during fast charging. J. Power Sources 2019;412:204–23. https://doi.org/10.1016/j.jpowsour.2018.11.043.

[21] Erhard SV, Osswald PJ, Wilhelm J, Rheinfeld A, Kosch S, Jossen A. Simulation and measurement of local potentials of modified commercial cylindrical cells. J. Electrochem. Soc. 2015;162:A2707–19. https://doi.org/10.1149/2.0431514jes.

[22] Hales A, Marzook MW, Bravo Diaz L, Patel Y, Offer G. The surface cell cooling coefficient: a standard to define heat rejection from lithium ion battery pouch cells. J. Electrochem. Soc. 2020;167:020524. https://doi.org/10.1149/1945-7111/ab6985.

[23] Lander L, Kallitsis E, Hales A, Edge JS, Korre A, Offer G. Cost and carbon footprint reduction of electric vehicle lithium-ion batteries through efficient thermal management. Appl. Energy 2021;289:116737. https://doi.org/10.1016/j.apenergy.2021.116737.

[24] Marzook MW, Hales A, Patel Y, Offer G, Marinescu M. Thermal evaluation of lithium-ion batteries : defining the cylindrical cell cooling coefficient. J Energy Storage 2022;54:105217. https://doi.org/10.1016/j.est.2022.105217.

[25] Doyle M, Fuller TF, Newman J. Modeling of Galvanostatic charge and discharge of the lithium polymer insertion cell. J. Electrochem. Soc. 1993;140:1526–33. https://doi.org/10.1149/1.2221597.

[26] Smith K, Wang CY. Power and thermal characterization of a lithium-ion battery pack for hybrid-electric vehicles. J. Power Sources 2006;160:662–73. https://doi.org/10.1016/j.jpowsour.2006.01.038.

[27] Kumaresan K, Sikha G, White RE. Thermal model for a Li-ion cell. J. Electrochem. Soc. 2008;155:A164. https://doi.org/10.1149/1.2817888.

[28] Jokar A, Rajabloo B, Désilets M, Lacroix M. Review of simplified Pseudo-two-dimensional models of lithium-ion batteries. J. Power Sources 2016;327:44–55. https://doi.org/10.1016/j.jpowsour.2016.07.036.

[29] Kim G-H, Smith K, Lee K-J, Santhanagopalan S, Pesaran A. Multi-domain modeling of lithium-ion batteries encompassing multi-physics in varied length scales. J. Electrochem. Soc. 2011;158. https://doi.org/10.1149/1.3597614.

[30] Haug M, Noel A, Wilhelm J, Thoennessen T, Rheinfeld A, Jossen A. Simulation and measurement of the current density distribution in lithium-ion batteries by a multi-tab cell approach164; 2017. p. 6324–33. https://doi.org/10.1149/2.0551701jes.

[31] Rieger B, Erhard SV, Kosch S, Venator M, Rheinfeld A, Jossen A. Multi-dimensional modeling of the influence of cell design on temperature. Displacement and Stress Inhomogeneity in Large-Format Lithium-Ion Cells 2016;163. https://doi.org/10.1149/2.1051614jes.

[32] Kosch S, Zhao Y, Sturm J, Mulder G, Ayerbe E, Jossen A. A computationally efficient multi-scale model for lithium-ion cells165; 2018. p. 2374–88. https://doi.org/10.1149/2.1241810jes.

[33] Newman J, Tiedemann W. Porous-electrode theory with battery applications. AICHE J. 1975;21:25–41. https://doi.org/10.1002/aic.690210103.

[34] Gu H. Mathematical-analysis of a Zn/Niooh cell. J. Electrochem. Soc. 1983;130:1459–64. https://doi.org/10.1149/1.2120009.

[35] Kwon KH, Shin CB, Kang TH, Kim C-S. A two-dimensional modeling of a lithium-polymer battery. J. Power Sources 2006;163:151–7. https://doi.org/10.1016/j.jpowsour.2006.03.012.

[36] Kim US, Shin CB, Kim C-S. Effect of electrode configuration on the thermal behavior of a lithium-polymer battery. J. Power Sources 2008;180:909–16. https://doi.org/10.1016/j.jpowsour.2007.09.054.

[37] Soltanali H, Rohani A, Tabasizadeh M, MHA Fard, Parida A. Int J Automot Eng 2018;8:2781–91.

[38] Madani SS, Swierczynski M, Kær SK. Cooling simulation and thermal abuse modeling of lithium-ion batteries using the Newman, Tiedemann, Gu, and Kim (NTGK) model. ECS Trans. 2017;81:261–70. https://doi.org/10.1149/08101.0261ecst.

[39] Chen SC, Wan CC, Wang YY. Thermal analysis of lithium-ion batteries. J. Power Sources 2005;140:111–24. https://doi.org/10.1016/j.jpowsour.2004.05.064.

[40] Liu Y, Liao YG, Lai M-C. Transient temperature distributions on lithium-ion polymer SLI battery. Vehicles 2019;1:127–37. https://doi.org/10.3390/vehicles1010008.

[41] Veth C, Dragicevic D, Pfister R, Arakkan S, Merten C. 3D electro-thermal model approach for the prediction of internal state values in large-format lithium ion cells and its validation. J. Electrochem. Soc. 2014;161:A1943–52. https://doi.org/10.1149/2.1201412jes.

[42] Inc Tesla. Battery Day video. https://www.youtube.com/watch?v=l6T9xIeZTds; 2020 (Accessed 11 June 2023).

[43] Zhao Y, Patel Y, Zhang T, Offer GJ. Modeling the effects of thermal gradients induced by tab and surface cooling on lithium ion cell performance. J. Electrochem. Soc. 2018;165:A3169–78. https://doi.org/10.1149/2.0901813jes.